Modeling the atmospheric dust cycle: 2-Simulation of Saharan dust sources

Beatrice Marticorena, G. Bergametti, B. Aumont, Yann Callot, Claude N'Doumé, Michel Legrand

JOURNAL OF GEOPHYSICAL RESEARCH, VOL. 102, NO. D4, PAGES 4387–4404, FEBRUARY 27, 1997

Modeling the atmospheric dust cycle 2. Simulation of Saharan dust sources

B. Marticorena, G. Bergametti, and B. Aumont
Laboratoire Interuniversitaire des Systèmes Atmosphériques, Créteil, France

Y. Callot
Laboratoire de Télédétection, Tours, France

C. N'Doumé and M. Legrand
Laboratoire d'Optique Atmosphérique, Lille, France

Abstract. A soil-derived dust emission scheme has been designed in order to provide simulation of mineral dust sources for atmospheric transport models [*Marticorena and Bergametti,* 1995]. This physical scheme considers the influence of surface features to compute the erosion threshold and the intensity of the dust emissions. It has been validated by comparison with relevant experimental data. However, it was necessary to extend its applicability and to test its capability to reproduce dust emissions over large arid areas. Specific methods have been developed to determine the parameters required by the dust production model for large-scale applications. The surface features (dimensions of the roughness elements and soil mineralogy) and the wind velocity allow the computation of the roughness lengths of the surface, the size distribution of the erodible soils, and the wind friction velocity. A map of these surface characteristics has been established for the western part of the Sahara. This map coupled to the Europan Center for Medium-Range Weather Forecast (ECMWF) surface wind fields are used to simulate dust emissions in this desert region. The simulated emissions have been compared to the Infrared Difference Dust Index (IDDI), determined by means of the Meteosat thermal infrared imagery. The simulated dust event frequencies are in good agreement with those observed by satellite. The comparison between the simulated fluxes and the satellite observations for 3 months of the year 1991 has revealed a linear relationship between the logarithm of the simulated flux and the IDDI. The annual and monthly dust emissions for 1991 and 1992 have been estimated and compared to those established by *d'Almeida* [1986]. Both the frequencies and the intensities of the emissions are well reproduced by the model associated with the surface features map.

1. Introduction

The simulations of the atmospheric dust cycle with Global Circulation Models (GCMs) for past and present conditions help in understanding how climatic changes and dust emissions interact. Until now, most of these simulations [*Joussaume*, 1990, 1993; *Genthon*, 1992; *Tegen and Fung*, 1994] have failed in reproducing both the intensity of dust emissions and the atmospheric concentration fields. The reasons most frequently invoked to explain these deficiencies are the parameterizations used to represent the emission processes [*Genthon*, 1992; *Joussaume*, 1990, 1993]. In these simulations the spatio-temporal heterogeneity of the dust emissions is mainly due to the variability of the wind velocity. However, field studies of erosion processes have shown that the surface features play an important role in both the location of the source regions and the intensity of dust emissions [*Gillette,* 1979; *Gillette et al.*, 1982; *Nickling*, 1988, 1994]. Indeed, the surface features control three major processes of dust production: the erosion threshold wind velocity, the wind shear stress acting on the erodible surface, and the capability of the soil to release fine dust particles. To improve GCM simulations of the desert dust cycle a physical dust emission scheme accounting for the influence of the surface features on the dust emissions has been developed [*Marticorena and Bergametti*, 1995]. The validations of this dust production model have established the physical consistency and the ability of the model to reproduce measurements of erosion thresholds and the dust fluxes for various conditions of the surface features.

Since this model was developed to simulate the desert dust cycle for a GCM, it is now necessary to extend its applicability to large scales and to test its capability to reproduce dust emissions over large arid areas. Thus this paper deals, first, with the methods developed to provide the input parameters required by this dust emission scheme on a scale compatible with a GCM and, second, with an evaluation of the quality of the large-scale dust emission simulations by comparison with satellite observations.

Paper number 96JD02964.
0148-0227/97/97JD-02964$09.00

2. Principles of the Dust Emission Model

Schematically, the model is composed of three main parameterizations representing (1) the erosion threshold wind friction velocity, (2) the total quantity of soil particles mobilized by wind (horizontal flux), and (3) the flux of fine dust particles emitted into the atmosphere (vertical flux).

2.1. Erosion Threshold Wind Friction Velocity

The aeolian erosion over a smooth erodible surface is the simplest case to consider. In this situation the aeolian shear stress is almost totally transferred to the erodible surface to initiate the soil particle motion. Thus the erosion threshold parameterization simply consists in determining the minimal wind velocity required to mobilize a soil grain of a given size.

A relation between the threshold wind friction velocity U^*_t and the soil particle diameter D_p has been derived from *Iversen and White's* [1982] expressions: for $0.03 < B < 10$,

$$U_t^*(D_p) = \frac{0.129\,K}{\left(1.928\ (aD_p^x + b)^{0.092} - 1\right)^{0.5}} \qquad (1)$$

for $B > 10$,

$$U_t^*\left(D_p\right) = 0.129\ K\left[1 - 0.0858\ \exp\left(-0.0617\left((aD_p^x + b) - 10\right)\right)\right] \qquad (2)$$

$$K = \left(\frac{\rho_p\ g\ D_p}{\rho_a}\right)^{0.5}\left(1 + \frac{0.006}{\rho_p\ g\ D_p^{2.5}}\right)^{0.5}$$

0.006 having units of g $cm^{0.5}$ s^2, B being the Reynold's number $B = U_t^*\ D_p / \nu$, ν the air kinematic viscosity, ρ_p and ρ_a the particle and the air density, respectively ρ_p= 2.65 g cm^{-3}, ρ_a=0.00123 g cm^{-3} and ν=0.157 cm^2 s^{-1}, a=1331 cm^{-x}, b=0.38, and x=1.56, b and x being dimensionless.

Since the threshold wind friction velocity does not vary linearly with the particle diameter in these expressions and because various grain sizes coexist in a given soil, the soil size distribution must be characterized by a continuous statistical function. This function represents the size distribution of the in situ erodible soil particles in their natural state of aggregation.

The problem of the erosion threshold on rough surfaces is more complex, since the wind shear stress is partitioned between the roughness elements and the erodible surface, leading to an apparent increase of the threshold wind friction velocity. A drag partition scheme has been developed to quantify the fraction of the total wind shear stress acting on the erodible surface to mobilize the soil particles [*Marticorena and Bergametti*, 1995]. This partition scheme expresses the ratio of total wind friction velocity U^* to the wind friction velocity on the erodible part of the surface U_s^*. This scheme uses the roughness lengths of the rough surface Z_0 and of the erodible part of the surface z_{0s} as unique parameters:

$$f_{\text{eff}} = \frac{U_s^*}{U^*} = 1 - \left(\frac{\ln\left(Z_0 / z_{0s}\right)}{\ln\left(0.35\left(10 / z_{0s}\right)^{0.8}\right)}\right) \qquad (3)$$

where Z_0 and z_{0s} have units of centimeters.

This partition scheme has been validated by comparison with shear stress partition measurements performed in wind tunnel for a large range of overall roughness lengths [*Marshall*, 1971] and various smooth roughness lengths [*Alfaro and Gomes*, 1995].

Combining the relation between U_s^* and D_p with the partition scheme provides a parameterization of the threshold wind friction velocity for any surface submitted to erosion:

$$U_t^*(D_p; Z_0; z_{0s}) = \frac{U_{ts}^*(D_p)}{f_{\text{eff}}(Z_0, z_{0s})} \qquad (4)$$

This parameterization of the threshold wind friction velocity has been tested by comparison with wind tunnel measurements [*Gillette et al.*, 1982; *Nickling and Gillies*, 1989] performed on various natural sites ranging from smooth erodible surfaces to surfaces totally protected from erosion [*Marticorena and Bergametti*, 1995].

2.2. Horizontal Flux *G*

This size-dependent expression of the threshold wind friction velocity has been included in a flux formulation proposed by *White* [1979] to calculate the vertically integrated horizontal flux G. G represents the total quantity of material in movement in the saltation layer. This parameterization of G accounts for the selective mobilization of the soil particles according to their size and computes the specific contribution of each size range to the total flux. The total horizontal flux is then defined as the sum, over the size distribution of erodible particles, of the individual size class contributions, weighted by their areal abundance. The areal abundance of each size range is expressed as their relative areal surface, which is computed from the statistical lognormal function characterizing the erodible soil mass size distributions. Thus the final expression of the horizontal flux is

$$G_{\text{tot}} = E\ \frac{\rho_a}{g}\ U^{*3} \int_{D_p} \left(1 + R\right)\left(1 - R^2\right)\ dS_{\text{rel}}(D_p)\ dD_p \qquad (5)$$

where E is the ratio of erodible to total surface, $dS_{rel}(D_p)$ is the relative surface covered by the particles of diameter D_p, $\int dS_{rel}(D_p)\,dD_p = 1$, U^* is the wind friction velocity, and

$$R = \frac{U_t^*\left(D_p, Z_0, z_{0s}\right)}{U^*}$$

The capability of such a size-dependent representation of the horizontal flux to reproduce the total mass and size distribution of the horizontal flux has been established by comparison with mass flux and size distribution of saltating particles measured in wind tunnels for various soil substrates and wind friction velocities [*Williams*, 1964; *Sörensen*, 1985].

2.3. Dust Flux *F*

Fine transportable dust particles (< 20 μm) are rarely present as loose particles in the soils. Owing to interparticle cohesion forces, their threshold wind friction velocities are so high that their motion could not be initiated directly by the wind. Saltation is a necessary intermediate process for dust production, dust particles being released by the impacts on the surface of the saltating particles. These impacts furnish the energy that allows the breakage of the soil aggregates [*Gomes et al.*, 1990a]. From wind tunnel observations, Shao et al. [1993] deduced that the dust flux F can be considered as a constant fraction (α) of the horizontal flux G. These authors proposed a theoretical expression for the ratio of vertical to horizontal flux $\alpha=F/G$. This ratio depends on the kinetic energy of the impacting particle (and thus of its size) and on the resistance of the surface to release fine particles (i.e., the potential energy linking the dust particles). Until now, the complexity of the involved processes has not allowed us to establish a physical parameterization to quantify the dust flux and to determine the size distribution of the emitted particles.

An empirical parameterization of the dust flux has been established. It is based on the assumption that the capacity of a soil to release fine particles depends on the abundance of these particles within the soil. The composition of the desert dust aerosol is largely dominated by clay minerals [*Glaccum and Prospero*, 1980; *Prospero et al.*, 1981]. Therefore it is reasonable to assume that the clay component of the soil constitutes the stock of available fine particles. A relationship was observed between the averaged ratio α and the soil clay content measured by *Gillette* [1979] for eight soils, whose clay content varies from 2 to 20%. So that the mass dust flux can be empirically estimated from the computed horizontal flux and the soil clay content.

To summarize, this model allows the computation of the dust flux produced by a given surface, provided that the required input parameters have been specifically determined. Two categories of parameters can be distinguished. First are those concerning the soil nature, including the size distribution of the erodible soil and the ratio of vertical to horizontal flux, α, depending on the soil type. Second are those relative to the surface roughness, which are mainly aerodynamic parameters: the wind friction velocity, U^*, the overall roughness length of the surface Z_0, the roughness length of the erodible part of the surface z_{0s}, and the erodible fraction of the surface E.

In practice, the applicability of this model at a large-scale is limited by the ability to determine the required input parameters on a scale compatible with GCM. Thus we have established relationships between the model input parameters and accessible data that will then be mapped over a test area.

3. Input Parameters

3.1. Access to the Input Parameters

3.1.1. Soil Parameters. The properties of the eroded soil influence dust emissions in two ways:

1. The soil size distribution controls the threshold wind friction velocity and the specific production rate for each size range of erodible particle.

2. The capacity of the soil to release fine transportable particle determines the intensity of the flux of emitted dust.

The dust emission model accounts for these two effects, if two soil characteristics are provided: (1) the soil size distribution, representing the size of the in situ erodible grains and aggregates, in the form of a continuous function and (2) the soil clay content, from which the ratio of vertical to horizontal flux α is computed.

In pedological maps the soils are generally referenced to the classical sedimentological textural triangle. The three vertices of this triangle (sand, silt, and clay) are defined by grain size: sand represents the size range 2000-80 μm, silt 80-4 μm, and clay >4 μm. In fact, clay is not really present in the natural soils in the form of loose grains. It is only observed when soils are submitted to wet sedimentation techniques, which lead to the breakage of aggregates by the polarizing effects of water. Because aeolian erosion acts on the soil aggregates, such a classification is not pertinent to characterize the properties of the erodible soil. An alternative approach consists in determining the size distribution of the soil aggregates by using dry techniques that minimize the breakage effects. Such an approach has been proposed by *Chatenet et al.* [1996] and is briefly summarized hereafter. It has been further improved to represent the ratio of vertical to horizontal flux α of the soils.

Size distribution: A set of 26 representative surface sediment samples (corresponding to the first five centimeters of the soil and often less) was collected in various arid and semiarid regions (Algeria, Niger, United States (California), Spain). Because soil aggregates larger than 1-2 mm are erodible only by extremely high winds, only size fractions smaller than 2 mm were measured by dry sieving. A fitting procedure was used, based on the adjustment of lognormal distributions to the measured mass size distribution. The fitting procedure minimized the difference between the simulated and observed populations for each size class [*Gomes et al.*, 1990b]. For three size fractions (<40, 40-100 and 100-250 μm) the 10 major elements (Na, Mg, Al, Si, P, Ca, K, Ti, Mn, Fe) were analyzed by Xray fluorescence.

By combining the soil size distributions and their elemental chemical composition, four populations were identified as typical components of the collected soils and characterized both from a size distribution and mineralogical point of view (Table 1). A typology of desert soils has been established which consists of representing any soil as a mixture of the four populations in various proportions. Thus a size distribution can be assigned to any soil according to its mineralogical type.

Ratio of vertical to horizontal flux α: Since we have assumed that a soil can be considered as a mixture of the four reference populations of Table 1, the knowledge of the ratio α

Table 1. Lognormal Size Distribution Parameter and Mineralogical Features of the Four Populations Identified in the Soils From Arid and Semiarid Regions [from *Chatenet et al.*, 1996]

Typology	Code	Mineralogical Feature	D_{med}, μm	σ
Alumino-silicated-silt	ASS	Clay minerals dominant	125	1.8
Fine sand	FS	Quartz dominant	210	1.6
Coarse sand	CS	Quartz	690	1.6
Salts	Sa	Salt and clay minerals	520	1.6

corresponding to each of these populations allows us to estimate α for any soil. The ratio of vertical to horizontal flux was found to depend on the soil clay content (equation (6)). Thus additional analyses were performed on selected samples of the collected soils to determine the fine particle content of the four typical populations, in order to estimate the corresponding ratio α for the four populations.

A wet sedimentation laser granulometer was used to measure the fine-particle content (< 5.8 μm) of seven samples that constituted the fine sand (FS) and alumino-silicated-silt (ASS) populations.

The averaged fine-particle content measured in the samples characterized by a single FS population is 3.6%. Such a value is consistent with that measured by *Gillette* [1979] for similar soil types (1, 2, 4, and 5) (Table 2). For these soils the averaged measured α varies from 1.7×10^{-6} to 3.5×10^{-6} cm^{-1}. However, since Gillette's measurements correspond to clay particles defined as $D_p < 1$ μm and our measurements correspond to the clay particles defined as $D_p < 5.8$ μm, a mean ratio $\alpha = 10^{-6}$ cm^{-1} has been assigned to the FS population (Table 3).

None of the selected samples is composed of a pure ASS population, but four are mixtures of FS and ASS. The total fine particles content of these soils can be expressed as the sum of the fine particles released by each population, weighted by their percentage in the soil:

$$F_{soil} = p_{ASS} \cdot F_{ASS} + p_{FS} \cdot F_{FS} \quad (6)$$

Since the fine particle content of the FS population has been previously estimated, the fine particle content of the ASS population can be derived from the total content of these soils:

Table 2. Fine-particle (<1 μm) Content of the Soils Studied by *Gillette* [1979] and Sedimentological Typology and Mean of the Measured Ratio of Vertical to Horizontal Flux

Soil	Clay Content (Particles < 1 μm), %	Texture	Mean Ratio α = F/G, cm^{-1}
1	3.5	fine sand	2.1×10^{-6}
2	3.5	fine sand	3.5×10^{-6}
3	10.0	silt	2.7×10^{-5}
4	1.8	fine sand	1.8×10^{-6}
5	5.9	fine sand	1.7×10^{-6}
6	19.0	silt	2.4×10^{-4}
7	8.8	silt	3.6×10^{-5}

Table 3. Estimated Fine-Particle (<5.8 μm) Content and Mean Ratio of Vertical to Horizontal Flux for the Four Population Characteristics of the Soils From Arid and Semiarid Regions

Typology	Estimated Clay Content, %	Mean Ratio α=F/G, cm^{-1}
ASS	9.7	1.0×10^{-5}
FS	3.6	1.0×10^{-6}
CS	0	1.0×10^{-7}
Sa	3.2	3.3×10^{-6}

$$F_{ASS} = \frac{\left(F_{soil} - p_{FS}\, F_{FS}\right)}{p_{ASS}} \quad (7)$$

The mean fine-particle content of this population is close to 10%, in agreement with Gillette's measurements for soils 3, 6, and 7. The α range for these soils is 2.4×10^{-4} to 3.6×10^{-5} cm^{-1}. For the same reasons concerning differences in definition of clay size, as explained above, a mean ratio of 10^{-5} cm^{-1} has been selected to represent the ASS population (Table 3).

None of the samples exhibiting CS and salty populations has been submitted to wet sedimentation; thus their α have been estimated from the literature. Based on flux measurements performed by *Nickling and Gillies* [1989] on coarse sand dunes, a very low value for α (10^{-7} cm^{-1}) has been assigned to the CS population. Such a value is consistent with the fact that coarse sands, resulting from long-term aeolian sorting, are generally composed of large quartz grains and contain few fine particles.

The salty population is composed of silt particles, cemented by salty components [*Breuninger et al.*, 1989; *Chatenet et al.*, 1996]. Using the proportions of sand and silt given by these authors, the fine-particle content of this population is estimated to be about a third of the fine-particle content of the ASS population. Thus a mean ratio α of 3×10^{-6} cm^{-1} has been assigned to this population.

Knowing the mean ratio α of each of the four typical populations, this parameter can be estimated for any soil considered as a mixture of these populations, by using the relation

$$\alpha_{soil} = \sum_{n_{type}} p_i\, \alpha_i \quad (8)$$

where α_i is the vertical to horizontal flux ratio of the population i and p_i represents its mass fraction in the soil.

3.1.2. Aerodynamic Parameters. The main aerodynamic parameters required by the dust production model are the wind friction velocity U^* and the surface roughness lengths Z_0 and z_{0s}. Based on an experimental characterization of the surface features in Tunisia, *Escadafal* [1989] proposed a classification of the different roughness scales observed in arid environments. Macro-roughness corresponds to large-scale features, such as boulders, dunes, large vegetation, and gullies... Meso-roughness integrates elements such as small-scale vegetation, ripples, or any obstacle having centimetric or decimetric dimensions. Micro-

roughness is determined by millimetric elements and depends on the soil morphology. The scales of roughness important for aeolian studies vary from centimeters to several meters [*Greeley et al.*, 1991]. The surface roughness length or aeolian roughness length is controlled by the meso-roughness, while the micro-roughness influences mainly the smooth roughness length z_{0s}.

The GCMs use roughness parameters, generally in the form of drag coefficients, to represent the momentum flux in the atmospheric boundary layer. They can be considered as equal to those controlling the heat fluxes [*Joussaume*, 1993] or deduced from the standard deviation of the topography or from the height of the vegetation [*Hansen et al.*, 1983]. However, they do not adequately represent the roughness scale to describe a surface process like aeolian erosion.

Since Z_0 depends on the size and spacing of the roughness elements on the surface [*Greeley et al.*, 1991], the aeolian roughness lengths can be deduced from the dimensions of the roughness elements.

Surface roughness length: The relation between the roughness length and the dimensions of the obstacles follows. The roughness elements are generally described by the roughness density:

$$\lambda = \frac{nbh}{S} \tag{9}$$

where n is number of roughness elements, b is mean breadth of the roughness elements, and h is mean height of the roughness elements.

Lettau [1969] proposed a linear relation between Z_0, λ and h, formally justified by *Wooding* [1973] for low roughness densities:

$$\frac{Z_0}{h} = \frac{\lambda}{2} \tag{10}$$

Theoretically, such a linear dependence should be observed until λ reaches a value of 0.1 to 0.3. The precise form of the function and the maximum of λ depend on the geometry of the roughness elements [*Raupach*, 1991].

In practice, when plotting the ratios Z_0/h measured for roughness elements of various forms and dimensions versus the roughness density (Figure 1), a similar behavior is observed despite the variety of roughness conditions. The experimental Z_0/h values vary linearly with λ until a maximum value of the order of 0.1, in agreement with Lettau's relation, and then remain almost constant for further increase in λ. Such a constant ratio for high roughness density is in agreement with the simple relationship $Z_0/h = 1/C$, C ranging from 7 to 30 [*Lettau*, 1969; *Greeley and Iversen*, 1985].

The linear relation between Z_0/h and λ has been adjusted for $\lambda < 0.11$ (with $r = 0.91$):

$$Z_0/h = 0.479\lambda - 0.001 \tag{11}$$

For $\lambda > 0.11$, Z_0/h was considered constant:

$$Z_0/h = 0.005 \tag{12}$$

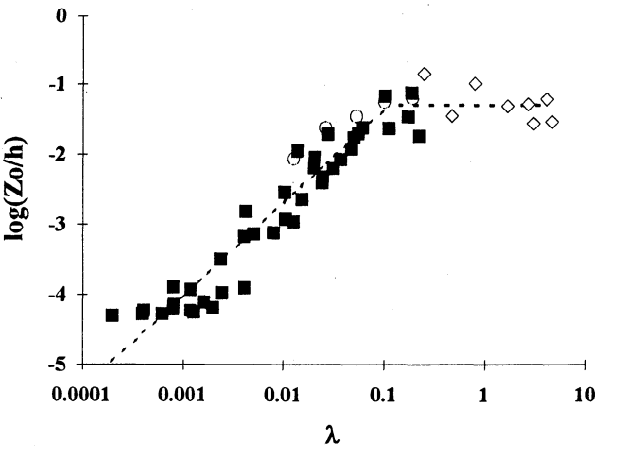

Figure 1. Variation of the ratio Z_0/h versus roughness density λ (squares, *Marshall* [1971] (cylinders and hemispheres of various size and spacing); diamonds, *Jarvis et al.* [1976], *Garratt* [1977], *Raupach et al.* [1991] (vegetation canopies and canopy models); circles, *Raupach et al.* [1980] (cylinders, h=0.6 cm and various spacing); dashed line, equations (11) and (12)).

These relationships allow calculation of the roughness length from the roughness density and the mean height of the roughness elements.

Escadafal [1989] observed in various sites of Tunisia that the pebbles were mainly ellipsoids of flatness 2/3, whose the frontal surface was approximately equal to half the surface they cover. This approximation is also acceptable for the kinds of persistent vegetation observed in semiarid areas, generally small bushes with low covering rates. The smallest roughness elements (gravel) were approximated to be spheres whose the roughness density was almost equivalent to the fraction of surface they cover. On the basis of these simple assumptions of the shape of the roughness elements, the roughness density can be deduced from the covering rate T (fraction of area covered) of the roughness elements and the roughness length from the covering rate of the roughness elements T and their mean height h.

Such a representation is adequate to describe surfaces characterized by a definite type of nonerodible elements, i.e., situations where the most abundant roughness elements absorb most of the wind momentum. The determination of the roughness length is more complex when sparse but large roughness elements produce a roughness length greater than that due to the most abundant nonerodible elements.

As an example, such situations occur in semiarid regions where inert non-erodible elements (rocks, pebbles, gravel) coexist with a sparse vegetation. In this case, the highest roughness length Z_{02}, induced by the largest roughness elements, controls the vertical wind velocity profile and thus the overall wind friction velocity. Nevertheless, the most frequent roughness elements induce an intermediate roughness level, characterized by a roughness length Z_{01}. This modifies the drag partition and thus influences the erosion threshold.

As mentioned above, a drag partition has been developed to determine the erosion threshold on rough surfaces characterized by a definite type of roughness elements: the surface boundary

layer is characterized by the overall roughness length Z_0 induced by the most frequent roughness elements, but an internal boundary layer, characterized by the smooth roughness length z_{0s}, develops over the erodible surface between two successive roughness elements. Assuming a logarithmic vertical profile of the wind velocity in the two boundary layers, the efficient fraction can be expressed as a function of the roughness length of the rough surface, of the erodible part of the surface, and of the height of the boundary layer δ.

$$f_{\text{eff}} = 1 - \left(\ln\left(\frac{z_0}{z_{0s}}\right) \Big/ \ln\left(\frac{\delta}{z_{0s}}\right) \right) \tag{13}$$

Based on experimental data, *Elliott* [1958] proposed the following equation to describe the variation of δ/z_{0s} with the distance x between two successive roughness elements.

$$\ln\left(\frac{\delta}{z_{0s}}\right) = 0.35\left(\frac{x}{z_{0s}}\right)^{0.8} \tag{14}$$

The sensivity of the partition scheme to the value of x has been evaluated from Marshall's drag partition measurements [*Marticorena*, 1995]. It has been found that for the simple case of a drag partition between the atmospheric boundary layer and the internal boundary layer the experimental data can be simulated well by using a single value X=10 cm. However, the best agreement between the computations and the measurements was obtained when $X = 1/D$, D representing the distance between the roughness elements.

The effect of the large but sparse roughness elements can be viewed as the addition of an upper boundary layer, characterized by the roughness length Z_{02}. The partition between this upper boundary layer and the intermediate one due to the most frequent roughness elements can be estimated by using the formulation of the drag partition between the erodible surface and these roughness elements.

Thus for these situations, a double-drag partition has been applied to express the efficient fraction F_{eff}, which represents the ratio of surface wind friction velocity to total wind friction velocity.

$$F_{\text{eff}} = f_{\text{eff}1}(Z_{01})\ f_{\text{eff}2}(Z_{02}) \tag{15}$$

Here, $f_{\text{eff}1}(Z_{01})$ describes the drag partition between the erodible surface and the most frequent roughness elements,

$$f_{\text{eff}1}(Z_{01}) = 1 - \left(\ln\left(\frac{Z_{01}}{z_{0s}}\right) \Big/ \ln\left(0.35\left(\frac{10}{z_{0s}}\right)^{0.8}\right) \right) \tag{16}$$

while $f_{\text{eff}2}(Z_{02})$ accounts for the partition between the two kinds of roughness elements:

$$f_{\text{eff}2}(Z_{02}) = 1 - \left(\ln\left(\frac{Z_{02}}{Z_{01}}\right) \Big/ \ln\left(0.35\left(\frac{X_{1-2}}{Z_{01}}\right)^{0.8}\right) \right) \tag{17}$$

Thus $f_{\text{eff}2}(Z_{02})$ is computed by using $X_{1-2} = d_{1-2}/3$, d_{1-2} representing the mean distance between two elements of each type.

Roughness length of the erodible surfaces z_{0s}: The smooth roughness length which represents the roughness induced by the soil grains on a bare erodible surface, is one parameter required by the drag partition scheme to compute the threshold wind friction velocity (equations (3) and (4)). *Marticorena and Bergametti* [1995] have shown that the sensitivity of the partition scheme to the smooth roughness length is such that a unique value of 10^{-3} cm for z_{0s} can be used to retrieve well the erosion threshold over a range of smooth roughness length varying from 10^{-4} to 3×10^{-3} cm. However, since the soil size distribution of the eroded soil is an input parameter of the dust production model, the median diameter of the coarser population of the soil size distribution $D_{P_{\max}}$ can also be used to determine the smooth roughness length. Thus the relation [*Bagnold*, 1941; *Greeley and Iversen*, 1985] between the roughness length of smooth erodible surfaces and the diameter of the erodible particles has been used:

$$z_{0s} = \frac{D_{P_{\max}}}{30} \tag{18}$$

Wind friction velocity. Classically, for stable surfaces of constant roughness length, the wind friction velocity is determined from the wind velocity and the roughness length, assuming a vertical logarithmic wind velocity profile [*Priesley*, 1959]: for $Z >> Z_0$

$$U(Z) = \frac{U^*}{k} \ln\left(\frac{Z}{Z_0}\right) \tag{19}$$

where $U(Z)$ is the wind velocity at the height Z, and Z_0 is the surface roughness length.

In GCMs, the wind velocity is computed for each grid mesh of the model, each time step, and each vertical level. The lowest level at which the wind velocity is computed is generally 10 m. Such a level seems sufficiently close to the surface to be compatible with the determination of the wind friction velocity in the surface boundary layer. Thus the wind velocity at 10 m will be considered as the joining point of the large-scale wind profile simulated by the GCM and controlled by the large-scale roughness parameters and the surface wind profile driven by the aeolian roughness length. Thus assuming a neutral stratification of the atmosphere, the wind friction velocity can be computed by using equation (17) from the wind velocity at 10 m and the aeolian roughness length.

For winds smaller than the erosion threshold, the surface roughness is controlled by the roughness elements present on the surface. However, once the threshold is reached, the saltating particles, having contacts with both the surface and the air, remove momentum from the air and transfer that momentum to the surface. Thus they offer a resistance to the wind which is comparable to the resistance due to the roughness elements. During saltation, the roughness can increase up to an order of magnitude [*Bagnold*, 1941; *Wieringa*, 1993]. This leads to a

significant modification of the wind velocity profile and thus of the wind friction velocity, referred to as the saltation wind friction velocity, U^*_{salt}.

Various theoretical approaches, mainly based on wind tunnel observations, have been developed to described this phenomenon [*Owen*, 1964; *Raupach*, 1991; *McEwan and Willetts*, 1993]. Assuming the roughness length of the saltation layer proportional to the square of the wind friction velocity, *Owen* [1964] proposed an expression of the saltation roughness length, which is similar to *Charnok*'s [1955] model for water surface roughness:

$$Z_{0salt} = c\frac{U^{*2}_{salt}}{2g} \tag{20}$$

where c is an empirical constant and g is the gravitational acceleration. This expression, established for smooth sand surfaces, implies a sudden change in the roughness length, once the erosion threshold is reached.

Based on an analogy with vegetation canopies, *Raupach* [1991] proposed an analytical expression for the saltation roughness length accounting for the continuity of the roughness length before and after the erosion threshold:

$$Z_{0salt} = \left(A\frac{U^{*2}}{2g}\right)^{\left(1-\sqrt{r}\right)}(Z_0)^{\sqrt{r}} \tag{21}$$

with

$$\sqrt{r} = U^{*2}_t / U^{*2} \text{ for } U^* \geq U^*_t \text{ and } \sqrt{r} = 1 \text{ if } U^* \leq U^*_t$$

A is equivalent to c in Owen's equation.

Raupach's relation agrees with *Rasmussen et al.*'s [1985] field experiments and with numerical models of the saltation process [*Raupach*, 1991]. It tends to Owen's expression for high wind velocities, but it provides a continuous increase of the roughness length from its initial static value in agreement with experimental observations (M. Sabre and L. Gomes, personal communication, 1996). However, the main strength of this formulation is that it can be applied to any surface, smooth or rough. For this reason, it has been used to compute the saltation wind friction velocities in our simulations.

From a practical point of view, its application requires an adequate U^*_t to use in equation (19). Indeed, Raupach's formulation has been established for the theoretical case of single-sized saltating particles, while natural soils are composed of particles of various size, selectively mobilized. Assuming that the saltation flux is mainly composed of the most easily mobilized particles, the U^*_t included in Raupach's formulation was selected to correspond to this size range. According to equations (1) and (2), the optimum particle diameter is about 80 μm, but for particles ranging from 60 to 120 μm, which are abundant in almost all soil types, the threshold wind friction velocity remains quite constant and close to 21 cm.s^{-1}. This value has been retained as the U^*_t to be included in equation (19). For rough situations this minimal velocity is weighted by the efficient fraction :

$$U^*_{t\,min} = \frac{U^*_t\left(D_{p_{opt.}}\right)}{f_{eff}\left(Z_0, z_{0s}\right)} \tag{22}$$

In this way, Raupach's formulation can be applied to any soil and any surface roughness.

The practical application of this formulation also required a numerical expedient. For a given roughness length and wind friction velocities ranging from 1 to 300 cm s^{-1}, the wind velocity at 10 m height, U(10m) is computed assuming a logarithmic wind profile. The wind friction velocity U^* is then adjusted to fit a polynomial function of degree 3 of U(10m) :

$$U^*_{salt} = a_0 + a_1 U(Z) + a_2 U^2(Z) + a_3 U^3(Z) \tag{23}$$

The error on the wind friction velocity (in cm s^{-1}) caused by equation (23) is of the order of one tenth of a centimeter.

To summarize, the saltation wind friction velocity is computed by using *Raupach*'s [1991] formulation as a function of the 10 m wind velocity, U(10m), and of the initial surface roughness length Z_0. It must be noted that this computation requires no additional parameter to the initial dust production scheme.

3.2. Determination of the Input Data.

The data that must be determined for the large-scale application of the dust emission scheme are the wind velocity at 10 m, the covering rate and mean height of the non erodible elements, and the mineralogical type of the soil. The zone selected for the large-scale application is the western part of the Sahara from 36°N to 16°N, and from 17°W to 12°E. This area represents 4,500,000 km^2 divided in grid meshes of a square degree.

3.2.1. Wind velocity. To perform the large-scale simulations of dust emissions, we have used here the analysed wind velocity fields of the European Centre for Medium Range Weather Forecasts (ECMWF) (Reading, UK) for the years 1991 and 1992. The wind velocities are instant values of the two horizontal components u and v of the horizontal wind, defined at 10 m, for 0000, 0600, 1200, and 1800 UT, with a resolution of 1.125°×1.125°. The norm of the wind velocity $(u^2+v^2)^{1/2}$ has been computed from u and v and interpolated to obtain a wind velocity field compatible with a square degree grid.

3.2.2. The geomorphologic approach. The method developed to map the surface features operates like a Geographical Information System (GIS) by aggregating refined data deduced from various sources of information to a larger scale and more general information.

The initial general information results from the examination of the topographical maps of the Saharan region provided by the French National Geographic Institute (IGN) for various scales (1/200,000, 1/500,000, 1/1,000,000). At this step, the principal landscape units can be distinguished on the topographic maps.

For this region, five main types of landscapes have been observed, corresponding to mountains, ergs, hamadas, plains and depressions, which are briefly described in Table 4. From orographical (topographical and hydrological) considerations, various general surface features can be associated to each type of landscapes. These surface features are defined in Table 5, and Table 6 summarizes the possible associations between the landscape type and the surface features.

A regional analysis of the orographic context is then performed by examining the relations between a grid mesh of one degree square and its neighbors in relation to a larger landscape unit (of the order, at least, of 12 degrees square). This regional analysis allows the selection of the relevant surface features associated with each landscape unit and the interpretation of the spatial variations in the surface features in relation with the process(es) responsible for their formation. For example, the fluvial and alluvial transport patterns result in a selective deposition of the pebbles, whose size decreases with an increase in the distance from the parent mountains. Therefore the gradient of the pebble size can be estimated by examining the positions of each area relative to the location of the source of these pebbles. For the dune fields, direct information about the form of the dune is reported on the topographical maps. A geomorphologic relationship is then used to estimate the size of the sand grains based on the form of the dunes [*Callot*, 1987]. The soil type in the dune fields can therefore be directly mapped based on topographical maps. More generally, this method relates regional information to local information from the effects of allochthonous processes acting on the surface features. This orographical approach is then improved by information resulting from both geologic and climatological analysis of the region.

Geological analysis: The geological analysis provides information on the surface features due to processes acting over timescales greater than 10^3 years. For example, the lithologic substratum of the surface represents the ancient surface material, whose weathering has led to the present soil mineralogy and roughness characteristics. It depends on the genesis, weathering, and erosion of the large topographic units. Both mineralogy and the size of the soil grains are strongly connected to the type of the parent rocks [*Dutil*, 1971]. The lithological analysis also provides information on the formation and structures of surface exhibiting large roughness, since the vulnerability of rocks to be weathered and broken controls the size of the resulting pebbles.

Table 5. General Surface Features Observed in the Western Part of the Sahara

Surface Feature	General Characteristic
Rocks	Rocky or skeletal soil, with large blocks
Reg	Stony surface with obstacles greater than 5cm and of variable density
Serir	Continuous surface with small pebbles and gravel smaller than 3 to 4 cm
Fluviatil deposit	Flat clayey silty stretch, possible gravel
Dunes	Sandy structure of variable slope
Sand sheets	Centimetric sandy sheet covering the whole surface
Daïa	Sedimentary silty clayey deposit
Sebkha	Sedimentary salty deposit, with various surface features according to the salt content and the salt nature

Climatological analysis: Many of the present surface features result from processes that were efficient in the past, when the climatic conditions were quite different than at present. As an example, the Sahara has experienced wetter periods, particularly during the recent Holocene (from 10,000 to 3500 years B.P.). The rivers were numerous and active, allowing transportation of larger pebbles [*Chavaillon*, 1964; *Conrad*, 1969]. Many lakes appeared during this period, especially in the northern Sahara [*Callot and Fontugne*, 1992; *Petit-Maire*, 1989; *Petit-Maire and Riser*, 1983], producing specific deposits when the climate became dryer. Some lakes previously supplied by streams loaded with detritic sediments became clayey plains with smooth surfaces. Paleolakes, fed by superficial gypseous water, became embossed topography, sensitive to weathering. The present surface features of the ancient or still active "sebkhas" vary, depending on their salt content and on the experienced periods of drying and moistening. These wet conditions have also enhanced the weathering and pedogenesis of the lithologic subtratum, producing large proportions of fine transportable material.

The present climatological conditions have similar influence, the most important parameter being the precipitation rate, which controls both the present weathering and the vegetation cover. On the hamadas of the northern Sahara, we observed that the latitudinal gradient of erodible material is affected by the present climate. On the desert margins, where the precipitation rates are

Table 4. Five Types of Landscapes Observed on the Topographic Maps of the Western Part of the Sahara

Landscape Type	Definition
Mountain	High relief
Erg	Fields of jointed dunes or disrupted by sandy or stony places
Hamada	Plateau with hard summit layer
Plain	Flat stretch without hard summit layer and without river incision
Endorheic depression	Underleveled surfaces, arrival point of ancient or present endorheic flows and/or of water rising

Table 6. Possible Associations Between the Type of Landscapes and General Surface Features

	Mountain	Erg	Hamada	Plain	Endorheic Depression
Rocks	X				
Reg	X	X	X	X	
Serir		X	X	X	
Fluviatile deposit				X	X
Dunes		X			
Sand sheets		X	X	X	
Daïa					X
Sebkha					X

of the order of 80 to 100 mm/yr, hamadas exhibit a low density of pebbles with large surface covered by fine material, while 150 km to the south, where the precipitation ranges only between 40 and 50 mm/yr, the surfaces are almost entirely covered by gravel, pebbles, and very coarse sand.

The most easily observed effect of precipitation concerns the seasonal vegetation cover. To avoid any uncertainty due to the representation of the temporal variability of the vegetation cover, the selected zone excluded the Sahelian belt. North of the Sahara, the area having a seasonal drift of the vegetation cover is limited, since the Atlas Mountains induce a sudden shift between desert and wetter regions. Thus only the permanent vegetation was considered and directly mapped. This was done by accounting for both the latitudinal and longitudinal gradients of precipitation rates [*Dubief*, 1963]. When precision was needed for some regions, complementary information like bibliographic documents, monographic studies, airborne photographs, soil maps of Africa [*d'Hoore*, 1963] and technical reports were examined.

Quantification: This geomorphologic approach allows us to establish a semiquantitative information system, since the surface characteristics in each square degree are only known relative to the neighboring grid meshes composing the same landscape unit. To be quantitative, the method needs aggregation of quantitative information on the surface properties. These quantitative references were provided by numerous direct observations performed in the selected region: in the northern Sahara, western and eaastern great sand seas, Atlasic hamadas, plateau of the Ghardaïa region, and low Sahara [*Callot*, 1988, 1992; *Callot and Fontugne*, 1992]; in the central Sahara, ergs around Tassilis N'Ajjers (Issaouane, N'Inarraren, Issaouane N'Tifernine), large fluvial areas (Taffassasset, Sebkha Mekkherane), Hoggar, southern Tassilis, and Ténéré; in the meridional Sahara, Aïr and erg of Bilma [*Mainguet and Callot*, 1979]; and in the western Sahara, the area of Tarfaya-Laayoune [*Callot and Oulehri*, 1996].

These "ground truths" have been used as adjustment points: for representative areas, the surface features (mean height and covering rate of the roughness elements; soil mineralogy) were precisely and quantitatively described and then used to calibrate the whole geomorphologic information system.

3.2.3. Surface feature maps. Each grid mesh is characterized by up to five surface feature types and the surface fraction covered by each of them in the grid mesh. However, these features were not geographically localized inside the grid mesh. Indeed, since the wind velocity is given for a square degree mesh, a unique value of the dust flux is computed for each grid mesh. This global dust flux is the sum of the flux produced by the various surface features weighted by the fraction they represent in the grid mesh. In this way, the heterogeneity of the surface features is accounted for with a resolution finer than a square degree, but not explicitly and spatially represented.

Soil type maps: Eight soil types have been used for the cartography. Based on the typology exposed in section 3.1.1 (Soil Parameters), a size distribution and a value of the ratio of vertical to horizontal flux, α, has been affected to each of these eight soil types. The statistical parameters of the lognormal mass size distributions and the values of the soils are listed in Table 7.

Figure 2 represents the percentage of the total area covered by each of these soil types. The dominant soil type, the coarse medium sand (CMS) spreads homogeneously over large areas and is associated to specific landscape units such as regs or hamadas. The coarse and fine sand (CS, FS) are located in the same areas, mainly those corresponding to the dune fields (ergs). They respectively represent 18% and 11% of the total area. Low surface fractions of these sands and of medium sand (MS) are spread over the entire regions, representing films of sand moving on the surface. The silty fine sand (SFS) corresponds to ancient alluvial or fluvial depressions (daïas) and thus is mainly observed in the northern margin, where the precipitation rates were sufficient in the past to produce such deposits. This soil type covers 10% of the total surface but never constitutes the dominant soil type of a grid mesh. The medium silty sand (SMS), the salty soils (SEM and SEF) and the medium sand (MS) constitute minor soil types in the studied zone (of the order of a few percent). And lastly, 7% of the total surface (mountains, urban areas, etc.) were a priori considered as nonerodible surfaces.

Roughness maps: The roughness mapping consists of determining for each typical surface the most frequent roughness elements, their mean height and covering rate. About 40 different roughness types have been distinguished, classified into four classes: S refers to the presence of vegetation, R refers to inert roughness elements (pebbles, gravel), S+R represents the association of vegetation and inert obstacles, and L refers to smooth erodible surfaces. The percentage of the total surface occupied by each class is reported in Figure 3. For vegetation

Table 7. Size Distributions and Mean Flux Ratio of the Soil Types Used for the Cartography of the Surface Features in the Western Part of the Sahara

Typology	Code	Population 1			Population 2			Population 3			Mean Flux Ratio
		D_{med}, μm	σ	%	D_{med}, μm	σ	%	D_{med}, μm	σ	%	α= F/G, cm^{-1}
Silty fine sand	SFS	210	1.8	62.5	125	1.6	37.5				4.5×10^{-6}
Medium sand	MS	690	1.6	80	210	1.8	20	-	-	-	5.5×10^{-7}
Coarse sand	CS	690	1.6	100	-	-	-	-	-	-	1.0×10^{-7}
Coarse medium sand	CMS	690	1.6	90	210	1.8	10	-	-	-	3.3×10^{-7}
Fine sand	FS	210	1.8	100	-	-	-	-	-	-	1.0×10^{-6}
Silty medium sand	SMS	125	1.6	37.5	210	1.8	31.25	690	1.6	31.25	4.2×10^{-6}
Moderately salty silt	SEM	125	1.6	50	520	1.5	50	-	-	-	4.1×10^{-6}
Highly salty silt	SEF	520	1.5	75	125	1.6	25	-	-	-	3.1×10^{-6}

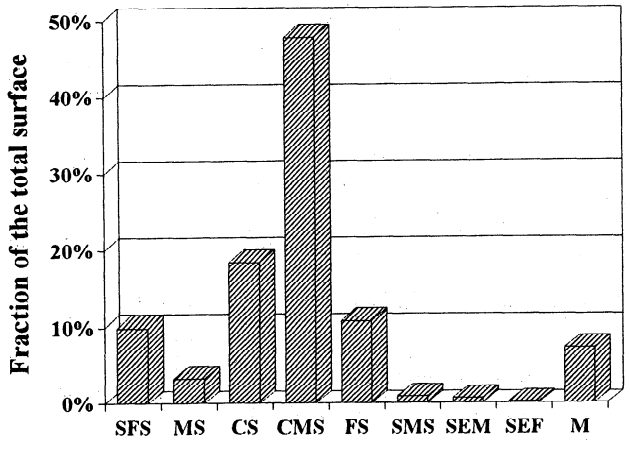

Figure 2. Fraction of the studied area covered by each soil type (SFS, silty fine sand; MS, medium sand; CS, coarse sand; CMS, coarse medium sand; FS, fine sand; SMS silty medium sand; SEM, moderately salty silt; SEF, highly salty silt; M, mountain, relief, urban area).

roughness the mean heights of the bushes are 10, 20, or 40 cm, with covering rates of 0%, 2%, 5%, 10%, or 20%. For inert obstacles the mean height varies from a few millimetres to about 10 cm, and five covering rates have been used: 0%, 5%, 10%, 20%, and 30%. The roughness length of the smooth surfaces is estimated from the median diameter of the coarser population constituting the soil. Based on the eight soil types used for the cartography (Table 7), three values of the smooth roughness length were used to characterize the smooth surfaces (0.0007, 0.0017, and 0.0023 cm). The mean height and covering rates of the nonerodible elements and relations (12) and (13) allow us to compute the roughness length from each roughness type.

Threshold velocities maps: Since the roughness of the surface controls the erosion threshold, the cartography of the roughness elements can be illustrated by the resulting maps of erosion thresholds. Each square degree is characterized by several surface features. Therefore it was not possible to report the corresponding threshold wind friction velocities on one map. Thus for sake of readability, we have computed the wind velocities at 10 m, for which a minimal dust flux is simulated by the model ($F > 10^{-13}$ g cm^{-2} s^{-1}) (Plate 1). Therefore this map illustrates the erosion threshold of the most easily mobilized fraction of the surface.

Except for the areas considered as nonsources, the threshold wind velocities are spatially highly variable but relatively homogeneous for a specific topographic unit. They range from 6.5 to 20 m s^{-1} with most of the values lower than 14 m s^{-1}. This range is consistent with the threshold wind velocities reported in the literature, 4 to about 20 m s^{-1} [*Pye*, 1987; *Helgren and Prospero*, 1987; *Nickling and Gillies*, 1989].

Finally, the input data used are wind speed, uniquely defined for a grid cell (1 degree square), and geomorphic type, defined as a fraction of the grid cell. There are several possible geomorphic types (up to five) for each cell. Each geomorphic type corresponds to a roughness length and a soil type. The sum of the geomorphic area fractions are the total area for each grid cell.

The dust flux computation is applied to each geomorphic type using the wind velocity of the cell considered. The sum of the dust fluxes emitted by each geomorphic type are the total dust flux of the grid cell, which is the final output of the model.

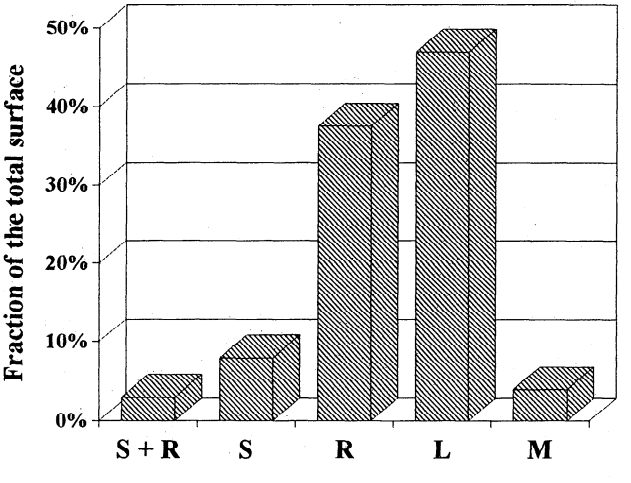

Figure 3. Percentage of the studied area covered by the roughness classes, S+R , vegetation and inert obstacles; S, vegetation; R, inert obstacles; L, smooth surfaces; M, nonerodible surfaces.

4. Validation of the Dust Flux Simulations

The evaluation of the capacity of the model to simulate the dust emissions correctly on large-scale requires validation data using a comparable scale. Using field measurements on such a large area was not considered to be practical. We chose satellite observations of desert dust to be the most adequate.

4.1. Comparison with Satellite Observations.

The atmospheric mineral dust induces a decrease of the solar radiation incoming on the surface. This leads to a decrease of the surface temperature and thus of the long-wave radiation emitted by the surface, which is further diminished while passing through the dust layer. These two effects produce a global decrease of the radiation measured in the infrared spectral range. This phenomenon is the basis of a method that was recently developed [*Legrand*, 1990; *N'Doumé*, 1993; *Legrand et al.*, 1994] to characterize the atmospheric dust content over the African continent using the thermal infrared channel (10.5 to 12.5 μm) of Meteosat satellites. The effect of the atmospheric mineral dust is calculated by correcting the initial signal of effects due to the continental surface, the atmospheric water vapor and the water clouds. To eliminate the effect of the surface and of the water vapor, a composite image (reference image) is established by selecting for each pixel the clearest observation (i.e., the highest radiometric levels) during a time period. The length of this period must be short enough to minimize bias due to temporal changes in the Sun position, the water vapor content, and the surface characteristics. The period must also be sufficiently long to select a maximum of clear pixels (free of dust or clouds). A

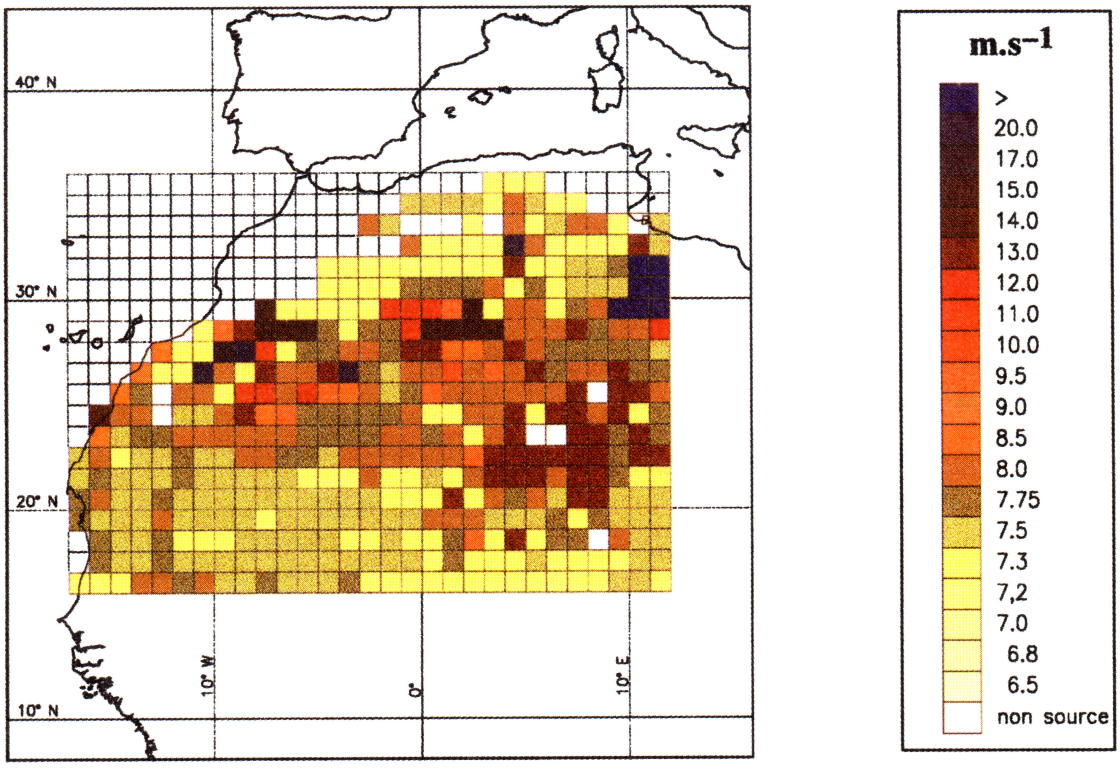

Plate 1. Threshold wind velocity defined at 10 m, computed from the surface feature maps.

period of 15 days was found to represent the best compromise. The reference image is then subtracted to the initial signal to provide a difference image containing only the effect of dust or water clouds. A statistical treatment derived from the spatial coherence method can be used to discriminate between water clouds (exhibiting pixels "colder" and more scattered than those corresponding to dust clouds) and dust clouds. The method consists of determining cutoff values for both the mean and the standard deviations on sets of running (3×3) pixels. Pixels containing water clouds are eliminated for further analysis. The information resulting from these successive treatments is a dustiness indicator: the Infrared Difference Dust Index (IDDI) expressed in Meteosat radiometric counts [*Legrand*, 1990]. These IDDI have not been quantitatively related to the vertically integrated dust content, mainly because of the lack of direct measurements of atmospheric dust content on such scale. However, a good relationship has been observed between the IDDI and horizontal visibility measurements from 39 African meteorological stations [*Legrand et al.*, 1994].

4.1.1 Dust event frequencies. To compare the simulated dust event frequencies to those deduced from satellite, a set of comparison criteria has been defined.

Comparison criteria. The atmospheric mineral dust detected by the satellite can be either locally emitted or transported from distant sources. The main problem for the comparison is to retain only the cases of locally emitted dust. In fact, there is a strong probability that the highest IDDIs are produced by local emissions and that, to the contrary, the lowest IDDIs mainly result from dust transport. Thus selecting the highest dust content by using an IDDI threshold represents a way to minimize the situations including dust transport without eliminating too many cases of intense dust emissions.

A dust event is generally characterized by a reduction of the horizontal visibility to about 1 km [*Middleton*, 1986]. Regarding the relation between the horizontal visibility and the IDDI [*Legrand et al.*, 1994], 30 radiometric counts correspond to a visibility of less than 1 km. Thus for the noncloudy pixels, we used a lower threshold of 30 counts to consider a pixel as a "dust source."

Using a high IDDI threshold also eliminates the local emissions of low intensity. Consequently, the simulated dust events of low intensity must also be removed from the comparison. Thus a dust flux threshold (10^{-10} g cm^{-2} s^{-1}) has been used to discard the lowest simulated emissions.

For the comparison to be more significant, a wind velocity threshold has been used to eliminate the situations of low wind velocity. Indeed, simulating no dust production when there is no wind is trivial for any dust production model. Such situations do not constitute a significant test of the capability of the model to correctly simulate dust events. This threshold wind velocity, $U(10\text{m}) = 4$ m s^{-1}, corresponds to the lowest wind velocity able to initiate a dust event [*Pye*, 1987; *Helgren and Prospero*, 1987].

For this comparison, 5 months have been selected, corresponding to various dust emission patterns in terms of emission intensity and of source location. March, May, and July correspond to high dust event frequencies, while January and November are characterized by few dust events of low intensity [*N'Doumé*, 1993].

It must be noted that dust was persistently observed in the latitudes 19° to 16°N, while the wind velocity remains very low.

This effect, which is particularly marked in summer, is interpreted as a barrier effect of the Intertropical Convergence Zone (ITCZ). Indeed, for 1991, the limit of the ITCZ varied from 15°N in spring to about 19°N in summer (Figure 4). The strong convergence that takes place in this region only allows the transport of dust in the latitudinal direction, leading to dust accumulation observable by satellite. Thus this area has been removed from the tested area, and the comparison of the dust events frequencies has been performed only for the region extending from 36°N to 19°N.

The consistence between the frequencies of dust events simulated by the model and observed by satellite is represented by a consistency index :

$$I_c = \frac{N(\text{observed dust / simulated dust}) + N(\text{clear sky / no simulated dust})}{N(\text{tested cases})} \quad (24)$$

This index expresses the ratio of the number of coinciding situations between simulations and observations to the total number of tested cases. A full agreement is obtained when I_c = 1; I_c= 0.5 indicates a random result, only one observation among two being correctly reproduced.

The comparison is performed day by day for each square degree. The consistency indexes were computed both on each degree over the 5 months and for each month over the whole area. The total number of tested cases is 22,904 and varies from 3547 in January to 5580 in March.

Consistency between the simulated and observed dust events: The consistency index obtained with the model have been compared to those produced, using the same comparison criterion, by a simple dust flux parameterization [*Tegen and Fung*, 1994] using a unique erosion threshold velocity over the whole area:

$$F = \kappa\, U^2(U - U_t) \quad (25)$$

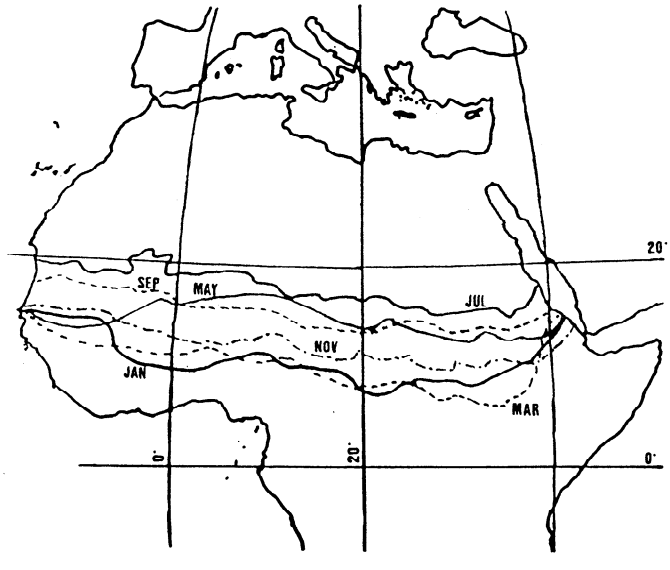

Figure 4. Variations of the location of the northern limit of the ITCZ during the year 1991 (from the Meteosat satellite image provided by Centre de Météorologie Spatiale, Lannion, France).

Table 8. Consistency Index I_c Obtained by Using Our Model and a Single-threshold Source Function for the Five Tested Months of 1991 and Their Averages

Tested Period	Number of Tested Cases	Consistency Index I_c	
		This Work	Equation (23)
January	3,547	0.77	0.57
March	5,580	0.76	0.60
May	5,265	0.79	0.60
July	4,742	0.78	0.56
November	3,770	0.89	0.71
Total	22,904	0.79	0.61

with U_t(10m) = 6.5 m s^{-1}.

This parameterization is similar to the one used in the most recent dust cycle simulation [*Tegen and Fung*, 1994], except that we used a unit value for κ, while Tegen and Fung made this parameter dependent on the soil texture. However, this difference does not have significant consequences on the comparison because it concerns only the dust event frequencies, while α acts on the emission intensities.

The consistency indexes averaged over the whole area are 0.79 for this model and 0.60 for the single-threshold source function. Such a difference is better illustrated when comparing the I_c averaged over the study area for each tested month (Table 8): the consistency index for this model remains higher than 0.75 and relatively stable over the five tested months, while it is only 0.60 for the single threshold function and varies from 0.56 in July to 0.71 in November, which is characterized by the lowest dust event frequency. These differences are further detailed in Figure 5, which represents the frequency spectrum of the I_c computed over the 5 months for each square degree. For this model the percentage of I_c higher than 0.7 is 74% but only 32% when using the single-threshold function; the indexes lower than 0.5 (no consistency with observations) are 1% for this model and 14% for the parameterization using a unique erosion threshold. Plate 2

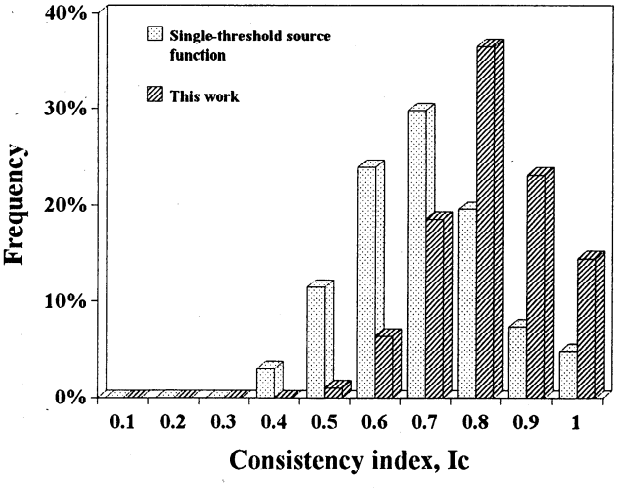

Figure 5. Frequency spectrum of the consistency index I_c obtained with this model and with a single-threshold source function (equation (23)).

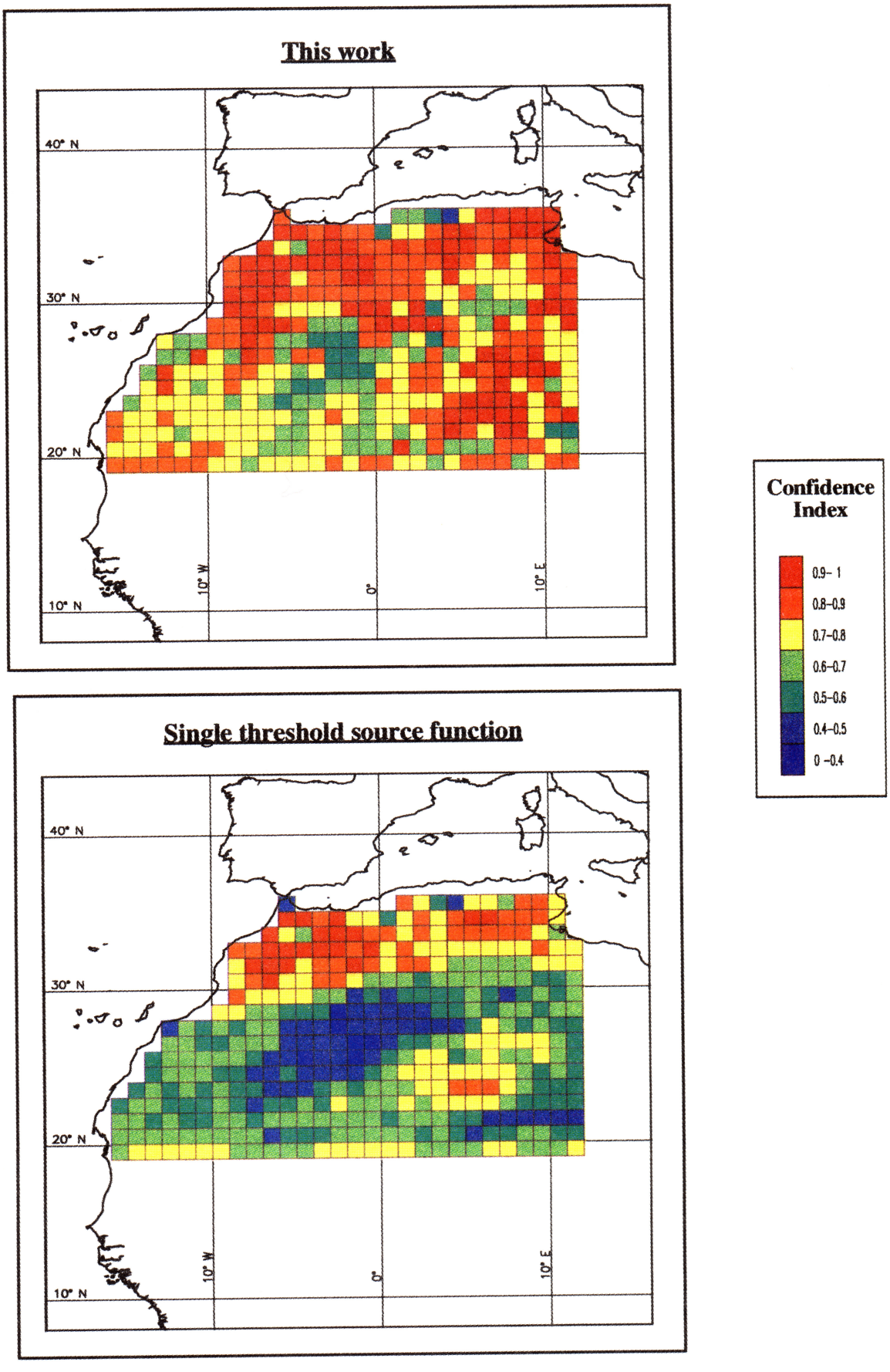

Plate 2. Maps of the consistence index I_c obtained with this model and by using a single-threshold source function (equation (24)).

shows that the improvement provided by the model applies to the whole area. In particular, the I_c are better in the center of the region, and the zone of I_c lower than 0.6 in the southeastern part is replaced by I_c of the order of 0.7. In the northern region the I_c were satisfactory when using the single-threshold source function, but the use of this model extended southward the domain of agreement.

These results confirm the idea that the spatio-temporal variability of the dust emissions is not only driven by the wind velocity variability, but strongly connected to the heterogeneity of the threshold wind velocity, and consequently, to the surface features in the source regions.

4.1.2. Comparison of the emission intensity with the IDDI. Although the IDDIs are only semiquantitative indicators of the atmospheric dust content, they have been complemented by the intensities of the simulated dust fluxes. To perform this quantitative comparison, we adopted an approach different from that for frequencies. Regarding the agreement between the simulated and observed dust event frequencies, we can assume that the IDDI corresponding to the cases where significant dust fluxes are simulated by the model, are mainly due to local emissions rather than to dust transport. Such an assumption is not rigorously fulfilled, in particular for the pixels close to areas of intense emissions, but appears sufficient to test the existence of a relationship between the simulated fluxes and the IDDI.

Thus we selected, without using any threshold, the IDDI corresponding to the cases where the model simulated fluxes higher than 10^{-11} g cm^{-2} s^{-1}, for the months where the dust emissions were the most intense (March, May, July). The range of IDDI from 0 to 50 counts has been divided in classes of 5 Meteosat counts wide. For each IDDI class, the mean simulated dust fluxes and the standard deviation σ have been computed. This comparison involved 3504 cases, the number of tested cases varying from 108 to 587 for the various IDDI classes.

The mean vertical fluxes have been plotted versus the mean IDDI of each class in Figure 6. The relationship observed between the logarithm of the simulated fluxes and the IDDI presents a high correlation coefficient and strongly suggests that the spatial distribution of the intensities of the simulated dust emissions is consistent with the satellite observations. However, because the IDDI are expressed in radiometric counts, this relation is only relative. Indeed, the same agreement should be obtained if the simulated fluxes were shifted by one or more order of magnitude. Thus we looked for supplementary quantitative constraint in the literature.

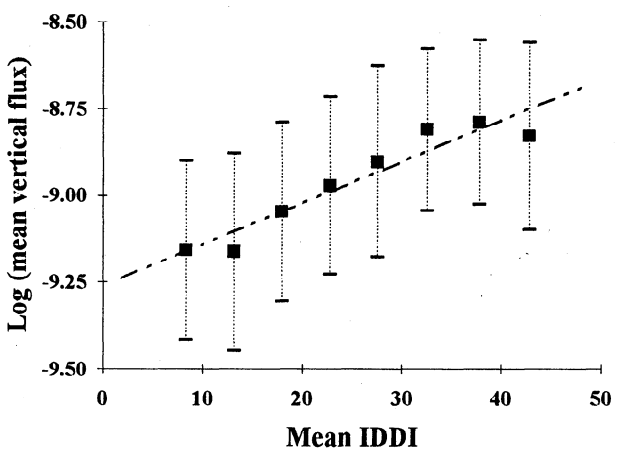

Figure 6. Relation between the mean vertical dust flux and the dustiness index for the months of March, May, and July of the year 1991 ($\log F = 0.012$ IDDI - 9.26; $r = 0.95$).

4.2. Comparison With Data From the Literature

From a quantitative point of view, two very different types of information to be compared with the results of our simulations are available in the literature. On one hand, the order of magnitude of the instantaneous simulated dust fluxes must be consistent with the dust fluxes measured locally in arid or semiarid regions. On the other hand, the integration of the simulated fluxes over the whole area must also be compatible with the available global estimations of the dust emissions in the Sahara.

4.2.1. Order of magnitude of the simulated dust fluxes. Dust flux measurements performed in Texas [*Gillette*, 1974, 1979] and Arizona [*Nickling and Gillies*, 1989] are in the range of 10^{-9} to 10^{-6} g cm^{-2} s^{-1}. Intense dust fluxes, of about 10^{-6} to 10^{-5} g cm^{-2} s^{-1} were measured in the delta of a river in the Yukon (Canada) [*Nickling*, 1978]. *Nickling and Gillies* [1993] have performed measurements on various sites in Mali, and observed dust fluxes 1 or 2 orders of magnitude lower than those measured in the United States. To summarize, the dust flux measurements provide a range between 10^{-12} and 10^{-5} g cm^{-2} s^{-1}, most of these values being centered around 10^{-9} to 10^{-8} g cm^{-2} s^{-1}. It is important to note that the aim of these field measurements is to quantify the dust flux emitted during significant dust events. The range of measured dust fluxes must be considered as reflecting the order of magnitude of relatively intense emissions rather than as representative of all dust emissions encountered in natural situations.

For the years 1991 and 1992, we have computed the frequency spectrum of the dust fluxes simulated daily at 0000, 0600, 1200 and 1800 UT. The frequency spectra are similar for these two years. Therefore we reported only the year 1991 in Figure 7. Most of the simulated fluxes are in the range of 10^{-11} to 10^{-9} g cm^{-2} s^{-1}. The spectrum exhibits a tail in the range of 10^{-9} to 10^{-6} g cm^{-2} s^{-1}, representing the most intense simulated events. The whole range of simulated fluxes is thus in agreement with the dust flux measurements reported in the literature, both in the lower and upper limits and, in particular, for the situations of intense emissions. This agreement demonstrates the relevance of the estimation the wind friction velocity developed for the large-scale application of the dust emission model.

4.2.2. Annual emissions and seasonal variability. *D'Almeida* [1986] has provided estimations of the annual and monthly dust emissions by the Sahara Desert. From a degradation soil maps (Food and Agriculture Organization), personal observations, and indications provided by local observers (meteorological stations), d'Almeida identified four principal dust source areas. Based on field measurements, the author related the angström turbidity coefficients to the concentrations of mineral dust and to the horizontal visibility, providing an empirical relationship between

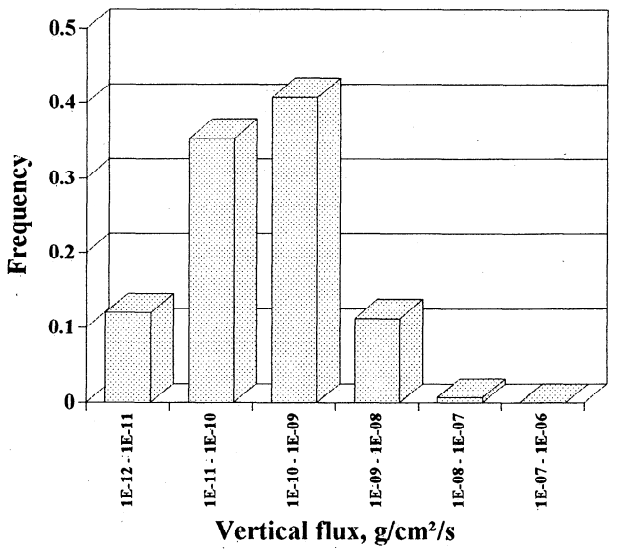

Figure 7. Frequency spectrum of the four-times-a-day simulated dust fluxes for the year 1991.

atmospheric dust concentration and the horizontal visibility. Considering that the visibility measurements performed in meteorological stations are representative of the dust emissions provided by the four identified source regions, he deduced the monthly emitted dust amounts from these sources. Summing the contribution of these four sources provides an estimation of the monthly and annual Saharan dust emissions for 1981 and 1982 (Table 9). Because these estimations were derived from direct measurements, they can be considered to be reliable in terms of amount of emitted dust. However, as mentioned by *Joussaume* [1990], the contribution to the total dust emissions of the sources located in the North-Sahara may be underestimated, since no sources were identified by d'Almeida in this region.

To compare the simulations with these estimations, we have computed the annual and monthly dust emissions for the years 1991 and 1992. These global emissions are based on the simulation of the dust flux for each square degree for the wind velocity at 0000, 0600, 1200, and 1800 UT derived each day from the ECMWF wind fields. The daily mean fluxes are computed by considering these instantaneous fluxes as representative of a 6-hour interval. The daily fluxes are averaged over the month and weighted by the surface area of the square degree to obtain monthly dust emission amount by square degree. These dust emission amounts are then averaged over the whole area to represent the monthly mean dust amount emitted by this part of the Saharan Desert (Table 10).

The annual simulated annual estimations are in excellent agreement with d'Almeida's estimations. Considering that d'Almeida's estimations are relative to the whole Sahara, it seems that the simulated emissions are slightly overestimated. However, the eastern source (A4) identified by d'Almeida does not contribute significantly to the total emissions: 1.6% in 1981 and 1.3% in 1982. Moreover, as previously mentioned no dust sources in the northern Sahara have been considered in these estimations. Consequently, the emission area accounted for by these two estimations can be considered as quite equivalent.

However, the monthly estimations provided by the two methods can vary significantly from one year to the other. Thus in order to minimize this interannual variability effect, we compared the monthly dust emissions averaged over 2 years, 1981 and 1982 for d'Almeida's estimations and 1991 and 1992 for ours (Figure 8). The seasonal patterns of the dust emissions are similar, with a maximum in March, a secondary maximum in summer, and very low emissions in winter, particularly from October and January.

The dust fluxes simulated by the model depend on the erosion threshold and on the wind friction velocity, but they are mainly controlled by the ratio of vertical to horizontal flux α. The reproduction of the monthly and annual emissions confirms the quantitative relevance of the parameterization of this ratio as a function of the soil type.

Table 9. Estimates of the Monthly and Annual Dust Amount Emitted by the Sahara Desert Proposed by *d'Almeida* [1986]

	Dust Emissions, Mt	
	1981	1982
January	26.1	36.5
February	68.6	77.5
March	99.0	120.1
April	89.6	72.7
May	67.6	67.6
June	86.2	92.6
July	41.6	66.7
August	40.3	59.2
September	27.2	48.5
October	15.8	28.3
November	24.1	20.7
December	41.5	22.3
Annual	627.5	712.8

Table 10. Estimates of the Monthly and Annual Dust Amount Emitted by the Western Part of the Sahara Desert, Based on the Dust Emissions Simulated by the Model Associated to the Surface Features Map for the Years 1991 and 1992

	Dust Emissions, Mt	
	1991	1992
January	23.5	25.0
February	71.9	73.3
March	163.0	101.0
April	53.0	66.5
May	72.1	77.8
June	48.9	56.2
July	60.6	65.1
August	44.7	51.2
September	31.1	24.1
October	24.0	18.7
November	25.8	19
December	44.5	8.4
Annual	665.0	586.4

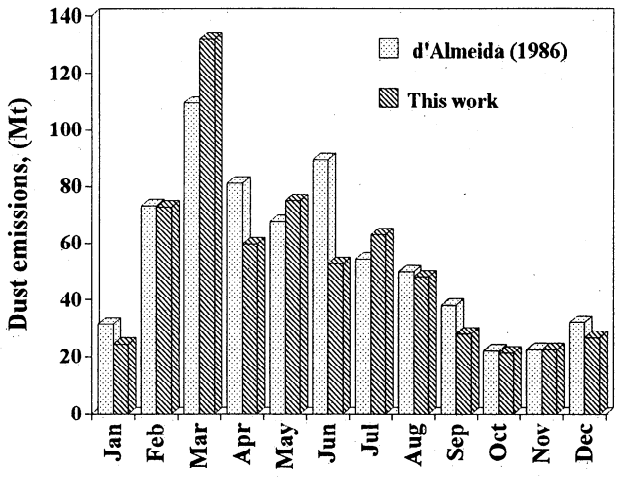

Figure 8. Variations of the monthly dust emissions as estimated by d'*Almeida* [1986] and as simulated by our model.

5. Conclusion

In order to simulate the desert dust cycle, a physical dust emission scheme has been designed, incorporating the influence of the surface features on dust emissions. The large-scale application of this physical scheme required us to establish additional parameterizations to estimate the input parameters from data accessible on such scales. A method has been developed for mapping these data on a test zone: the western part of the Sahara. The capability of this scheme to reproduce the dust emissions on a large-scale has been tested by comparison with dustiness index derived from Meteosat observations in the thermal infrared. The model using the maps of surface features reproduces the frequencies of dust events far better than those obtained by a single-threshold dust flux parameterization. These results emphasize that it is necessary to represent the heterogeneity of the erosion threshold in the source regions to simulate correctly the spatio-temporal variability of the dust event frequencies. A linear relationship has been established between the mean simulated dust fluxes and the IDDI, demonstrating the quantitative consistency between the intensity of the simulated dust fluxes and the satellite observations. Moreover, the simulated amounts of dust emitted annually and monthly were found to be in agreement with previous estimations based on field measurements. The model reproduces quite well both the amounts of emitted dust and the seasonal pattern of the dust emissions in the Sahara.

The validations performed by satellite observations and the available data from the literature constitute a body of evidence that confirms the capacity of the dust production model associated with the surface features map to reproduce the dust emissions. The inclusion of this model in a global circulation model is progressing and will lead to preliminary estimations of the local radiative effect of dust. This will constitute part three of this study of the atmospheric dust cycle.

Acknowledgments. This work has been supported by the Programme Environnement du CNRS in the framework of the program Erosion Eolienne en Régions Arides et Semi-arides. We particularly thank D.A. Gillette for his helpful and constructive comments. We would like to thank D. Dagorne from the Centre de Météorologie Spatiale (Lannion, France) for providing us the Meteosat images of the ITCZ over Africa.

References

Alfaro, S.C., and L. Gomes, Improving the large-modeling of the saltation flux of soil particles in the presence of nonerodible elements, *J. Geophys. Res.*, *100*, 16,357-16,366, 1995.

Bagnold, R.A., *The Physics of Blown Sand and Desert Dunes*, 265 pp., Methuen, New York, 1941.

Breuninger, R.H., D.A. Gillette, and R. Khil, Formation of wind-erodible aggregates for salty soils and soils with less than 50% sand composition in natural terrestrial environments, in *Paleoclimatology and Paleometeorology: Modern and Past Patterns of Global Atmospheric Transport*, edited by M. Leinen and M. Sarnthein, pp. 31-63, Kluwer., Nowell, Mass., 1989.

Callot, Y., Géomorphologie et paléoenvironnements de l'Atlas Saharien au Grand Erg Occidental: dynamique éolienne et paléolacs holocènes Université Paris VI, Thèse de Doctorat es Sciences, 412 pp, Paris, France, 1987.

Callot, Y., Evolution polyphasée d'un massif dunaire subtropical: le Grand Erg Occidental (Algérie), *Bull. Soc. Geol. Fr.*, *4-6*, 1073-1079, 1988.

Callot, Y., Paléolacs holocènes du nord du Grand Erg Occidental (NW du Sahara algérien), *Bull. Soc. Geol. Fr.*, *160*, 19-26, 1992.

Callot, Y., and M. Fontugne, Les étagements de nappes dans les paléolacs holocènes du nord-est du Grand Erg Occidental (Algérie), *C.R. Acad. Sci.,Ser. II, 315*, 471-477, 1992.

Callot, Y., and T. Oulehri, Géodynamique des sables éoliens dans le Nord-Ouest Saharien: Relations entre aérologie et morphologie, *Geodin. Acta*, *9*, n°1, 1-12, 1996.

Charnock, H., Wind stress on a water surface, *Q. J. R. Meteorol. Soc.*, *81*, 639-640, 1955.

Chatenet, B., B. Marticorena, L. Gomes, and G. Bergametti, Assessing the size distribution of desert soils erodible by wind, *Sedimentology*, *43*, 901-911, 1996.

Chavaillon, J., Etude stratigraphique des formations quaternaires du Sahara nord-occidental, Thèse de Doctorat es Sciences, 393 pp., *Ser. Geol. n°5*, Cent. Nat. Rech. Sci., Paris, 1964.

Conrad, J., L'évolution continentale post-hercynienne du sahara algérien, Thèse de Doctorat es Sciences, 527pp., *Ser. Geol. n°10*, Cent. Nat. Rech. Sci., Paris, 1969.

d'Almeida, G. A., A model for Saharan dust transport, *J. Clim. Appl. Meteorol.*, *25*, 903-916, 1986.

d'Iloore, J. L., Soil maps of Africa, sheets 4, 5, 6, *Joint Project 11*, Comm. for Tech. Coop. in Africa, Inter African Pedological Service, Inst. Geogr. Militaire, Brussels, Belgium, 1963.

Dubief, J., Le climat du Sahara, tome 2, fascicule 1, Mem. de l'Inst. de Rech. Sahariennes, 275 pp., Univ. d'Alger, Alger, 1963.

Dutil, P., Contribution à l'étude des sols et paléosols du Sahara, Thèse de Doctorat es Sciences, 346 pp., Univ. de Strasbourg, 1971.

Elliot, W.P., The growth of the atmospheric internal boundary layer, *Eos Trans. AGU, 39*, 1048-1054, 1958.

Escadafal, R., Caractérisation de la surface des sols arides par observations de terrain et télédétection, 317 pp., Collection Etudes et Thèses, ORSTOM, Bondy, France, 1989.

Garratt, J.R., Aerodynamic roughness and mean monthly surface stress over Australia, *Div. Atmos. Phys. Tech. Pap. 29*, Commonwealth Sci. and Land. Res. Organ., East Melbourne, Australia, 1977.

Genthon, C., Simulations of desert dust and sea-salt aerosols in Antarctica with a general circulation model of the atmosphere, *Tellus*, Ser. B, *44*, 371-389, 1992.

Gillette, D.A., On the production of soil wind erosion aerosols having the potential for long range transport, *J. Rech. Atmos., 8*, 735-744, 1974.

Gillette, D.A., Environmental factors affecting dust emission by wind erosion, in *Saharan Dust*, edited by C. Morales, pp. 71-94, John Wiley, New York, 1979.

Gillette, D. A., J. Adams, D. R. Muhs, and R. Khil, Threshold friction velocities and rupture moduli for crusted desert soils for the input of soil particles into the air, *J. Geophys. Res., 87*, 9003-9015, 1982.

Glaccum, R. A., and J.M. Prospero, Saharan aerosols over the tropical North Atlantic: Mineralogy, *Mar. Geol., 37*, 295-321, 1980.

Gomes, L., G. Bergametti, G. Coudé-Gaussen, and P. Rognon, Submicron desert dust: A sandblasting process, *J. Geophys. Res.,95*, 13,927-13,935, 1990a.

Gomes, L., G. Bergametti, F. Dulac, and U. Ezat, Assessing the actual size distribution of atmospheric aerosols collected with a cascade impactor, *J. Aerosol. Sci.,21*, 47-59, 1990b.

Greeley, R., and J.D. Iversen, *Wind as a Geological Process on Earth, Mars, Venus and Titan*, 333 pp., Cambridge Univ. Press, New York, 1985.

Greeley, R., et al., Radar-aeolian project, *NASA Rep. CR-4378*, 132 pp., 1991.

Hansen, J., G. Russell, D. Rind, P. Stone, A. Lacis, S. Lebedeff, R. Ruedy, and L. Travis, Efficient three-dimensional global models for climate studies : Models wind II, *Mon. Weather Rev., 111*, 609-662, 1983.

Helgren, D.M., and J. M. Prospero, Wind velocities associated with dust deflation events in the western Sahara, *J. Clim. Appl. Meteorol., 26*, 1147-1151, 1987.

Iversen, J.D., and B.R. White, Saltation threshold on Earth, Mars and Venus, *Sedimentology, 29*, 111-119, 1982.

Jarvis, P.G., G.B. James, and J.J. Landsberg, Coniferous forest in *Vegetation and the Atmosphere*, vol. 2, pp.171-240, edited by J.L. Monteith, Academic, San Diego, Calif., 1976.

Joussaume, S., Three-dimensional simulations of the atmospheric cycle of desert dust particles using a general circulation model, *J. Geophys., Res., 95*, 1909-1941, 1990.

Joussaume, S., Paleoclimatic tracers: An investigation using an atmospheric general circulation model under ice age conditions 1. Desert Dust, *J. Geophys. Res., 98*, 2767-2805, 1993.

Legrand, M., Etude des aérosols sahariens au-dessus de l'Afrique à l'aide du canal à 10 µm de Météosat: Visualisation, interprétation et modélisation, Thèse de doctorat es Sciences, 210 pp., Univ. Sci. Tech. de Lille Flandres Artois, 1990.

Legrand, M., C. N'Doumé, and I. Jankowiak, Satellite-derived climatology of the Saharan Aerosol, in *Passive Infrared Remote Sensing of Clouds and the Atmosphere II*, edited by D. K. Lynch, Proc. *Int. Soc. Opt. Eng., 2309*, 127-135, 1994.

Lettau, H.H., Note on aerodynamic roughness-parameter estimation on the basis of roughness element description, *J. Appl. Meteorol., 8*, 828-832, 1969.

Mainguet, M., and Y. Callot, L'erg de Fachi-Bilma (Tchad-Niger): Contribution à la connaissance de la dynamique des ergs et des dunes des zones arides chaudes, vol. 18,184 pp., *Mem. Doc. Cent. Nat. Rech. Sci.*, Paris, 1979.

Marshall, J.K., Drag measurements in roughness arrays of varying density and distribution, *Agric. Meteorol., 8*, 269-292, 1971.

Marticorena, B., Modélisation de la production d'aérosols désertiques en régions arides et semi-arides: développement et validation d'un code de calcul adapté au transport à grande échelle, Thesis, 268 pp., Univ. Paris VII Denis Diderot, 1995.

Marticorena, B., and G. Bergametti, Modeling the atmospheric dust cycle : 1 Design of a soil-derived dust emission scheme, *J. Geophys. Res.,100*, 16415-16430, 1995.

McEwan, I.K., and B.B. Willetts, Adaptation of the near-surface wind to the development of sand transport, *J. Fluid Mech., 252*, 99-115, 1993.

Middleton, N.J., A geography of dust storms in south-west Asia, *Int. J. of Climatol., 6*, 183-196, 1986.

N'Doumé, C., Traitement de l'imagerie Météosat IR pour l'observation des aérosols désertiques au dessus de l'Afrique: optimisation, validation et application à l'établissement des distributions spatio-temporelles, Thèse, 218 pp., Univ. Sci. Tech. de Lille Flandres Artois, 1993.

Nickling, W.G., Eolian sediment transport during dust storms : Slims River Valley, Yukon Territory, *Can. J. Earth Sci., 15*, 1069-1084, 1978.

Nickling, W. G., The initiation of particle movement by wind, *Sedimentology, 31*, 111-117, 1988.

Nickling, W. G., Aeolian sediment transport and deposition, in *Sediment Transport and Depositional Processes*, edited by K. Pye, pp. 293-350, Blackwell Sci., Cambridge, Mass., 1994.

Nickling, W.G., and J.A. Gillies, Emission of fine-grained particulates from desert soils, in *Paleoclimatology and Paleometeorology: Modern and Past Patterns of Global Atmospheric Transport*, edited by M. Leinen and M. Sarnthein, pp. 133-165, Kluwer Acad., Nowell, Mass., 1989.

Nickling, W. G., and J.A. Gillies, Dust emission and transport in Mali, West Africa, *Sedimentology, 40*, 859-868, 1993.

Owen, P.R., Saltation of uniform grains in air, *J. Fluid Mech., 20*, part 2, 225-242, 1964.

Petit-Maire, N., Interglacial environments in presently hyperarid Sahara: Paleoclimatic implications, in *Paleoclimatology and Paleometeorology: Modern and Past Patterns of Global Atmospheric Transport*, edited by M. Leinen and M. Sarnthein, pp. 637-661, Kluwer Acad., Nowell, Mass., 1989.

Petit-Maire, N., and J. Riser (Eds.), Sahara ou Sahel ? Quaternaire récent du bassin de Taoudenni (Mali), 473 pp., Cent. Nat. Rech. Sci and Ministère des Relations Extérieures, Imp. Lamy, 1983

Priesley, C. H.B., *Turbulent Transfer in the Lower Atmosphere*, 130 pp., Univ. of Chicago Press, Chicago, Ill., 1959.

Prospero, J. M., R.A. Glaccum, and R.T. Nees, Atmospheric transport of soil dust from Africa to South America, *Nature, 289*, 570-572, 1981.

Pye, K., *Aeolian Dust and Dust Deposit*, 334 pp., Academic, San Diego, Calif., 1987.

Rasmussen, K. R., M. Sörensen, and B.B. Willets, Measurement of saltation and wind strength on beaches, in *Proceedings of the International Workshop on the Physics of Blown Sand*, edited by O.E. Barndorff-Nielsen, J.T. Möller, K. Römer Rasmussen, and B.B. Willets, pp. 301-326, Univ. of Aarhus, Aarhus, Denmark, 1985.

Raupach, M.R., Saltation layers, vegetation canopies and roughness lengths, *Acta Mech., 1, Suppl*, 83-96, 1991.

Raupach, M.R., R.A. Antonia, and S. Rajagopalan, Rough-wall turbulent boundary layers, *Appl. Mech. Rev., 44*, 1-25, 1991.

Shao, Y., M.R. Raupach, and P.A. Findlater, Effect of saltation bombardment on the entrainment of dust by wind, *J. Geophys. Res., 98,* 12,719-12,726, 1993.

Sörensen, M., Estimation of some aeolian saltation transport parameters from transport rate profiles, in *Proceedings of the International Workshop on the Physics of Blown Sand*, edited by O.E. Barndorff-Nielsen, J.T. Möller, K. Römer Rasmussen and B.B. Willets, pp. 141-190, Univ. of Aarhus, Aarhus, Denmark, 1985.

Tegen, I., and I. Fung, Modeling of mineral dust in the atmosphere: Sources, transport, and optical thickness, *J. Geophys. Res., 99,* 22,897-22,914, 1994.

White, B.R., Soil transport by winds on Mars, *J. Geophys. Res., 84,* 4643-4651, 1979.

Wieringa, J., Representative roughness parameters for homogeneous terrains, *Boundary Layer Meteorol., 63,* 323-363, 1993.

Williams, G., Some aspect of the aeolian saltation load, *Sedimentology, 3,* 253-256, 1964.

Wooding, R.A., E.F. Bradley and J.K. Marshall, Drag due to regular arrays of roughness elements of varying geometry, *Boundary Layer Meteorol., 5,* 285-308, 1973.

B. Aumont, G. Bergametti and B. Marticorena, Laboratoire Interuniversitaire des Systèmes Atmosphériques, URA CNRS 1404, Université Paris VII et XII, Centre Multidisciplinaire de Créteil, 61 avenue du Général de Gaulle, 94010 Créteil cedex, France. (e-mail: aumont@univ-paris12.fr; bergametti@univ-paris12.fr; marticorena@univ-paris12.fr)

Y. Callot, Laboratoire de Télédétection, Université de Tours, Site Loire, BP 1028, 37012 Tours Cedex. (e-mail: callot@univ-tours.fr)

C. N'Doumé and M. Legrand, Laboratoire d'Optique Atmosphérique, USTL, bat. P5, 59655 Villeneuve d'Ascq Cedex. (e-mail: legrand@loa.univ-lille1.fr)

(Received February 3, 1996; revised July 28, 1996; accepted July 28, 1996.)